

# Relaxation-based dynamical Ising machines for discrete tomography

Mikhail Erementchouk, Aditya Shukla, Pinaki Mazumder

Department of Electrical Engineering and Computer Science, University of Michigan, Ann Arbor, 48104, MI, USA.

Contributing authors: [merement@gmail.com](mailto:merement@gmail.com); [aditshuk@umich.edu](mailto:aditshuk@umich.edu);  
[pinakimazum@gmail.com](mailto:pinakimazum@gmail.com);

## Abstract

Dynamical Ising machines are continuous dynamical systems that evolve from a generic initial state to a state strongly related to the ground state of the classical Ising model. We show that such a machine driven by the  $V_2$  dynamical model can solve exactly discrete tomography problems about reconstructing a binary image from the pixel sums along a discrete set of rays. In contrast to usual applications of Ising machines, targeting approximate solutions to optimization problems, the randomly initialized  $V_2$  model converges with high probability ( $P_{\text{succ}} \approx 1$ ) to an image precisely satisfying the tomographic data. For the problems with at most two rays intersecting at each pixel, the  $V_2$  model converges in internal machine time that depends only weakly on the image size. Our consideration is an example of how specific dynamical systems can produce exact solutions to highly non-trivial data processing tasks. Crucially, this solving capability arises from the dynamical features of the  $V_2$  model itself, in particular its equations of motion that enable non-local transitions of the discrete component of the relaxed spin beyond Hamming-neighborhood constraints, rather than from merely recasting the tomography problem in spin form.

**Keywords:** dynamical computations, combinatorial optimization, dynamical Ising machines, spin systems, discrete tomography, non-local transitions

## 1 Introduction

Ising machines represent an approach to computing that utilizes inherent properties of networks of classical spins, taking values  $\sigma = \pm 1$ . These computational properties

attract researchers' attention for a long time [1–4], and stem from two key properties of the Ising model ground state, the spin distribution with the lowest energy. First, the ground state can be regarded as solving a quadratic unconstrained binary optimization problem [5]. Second, by associating the spin distribution in the ground state with a partition of the graph nodes, one obtains the maximum (weighted) cut of the model graph [6]. Finding the maximum cut is an NP-complete problem [7, 8], which puts the Ising model into the general computing perspective [9].

The equivalence between the ground state and the max-cut problems follows from the following observation. Let the network of  $N$  classical spins be defined on a graph described by a weighted adjacency matrix with the matrix elements  $A_{m,n}$ . Regarding spin configuration (the distribution of spins on the graph)  $\sigma = (\sigma_1, \dots, \sigma_N)$  as a system of interacting spins as in the classical Ising model, we associate with  $\sigma$  an Ising energy

$$\mathcal{H}(\sigma) = \frac{1}{2} \sum_{m,n} A_{m,n} \sigma_m \sigma_n. \quad (1)$$

Alternatively, the spin configuration can be regarded as a designation of partition for individual graph nodes. For example, nodes with  $\sigma_n = 1$  and  $\sigma_n = -1$  are considered belonging to partitions 1 and 2, respectively. This defines a partition of the graph nodes that can be characterized by the weight of all cut edges, that is edges that connect nodes in different partitions. Introducing the cut indicator function  $\chi(m, n) = (1 - \sigma_m \sigma_n)/2$  for edge  $(m, n)$ , we obtain the cut function describing the spin configuration

$$\mathcal{C}(\sigma) = \frac{1}{4} \sum_{m,n} A_{m,n} (1 - \sigma_m \sigma_n). \quad (2)$$

Functions  $\mathcal{H}(\sigma)$  and  $\mathcal{C}(\sigma)$  are obviously related  $\mathcal{C}(\sigma) = \sum_{m,n} A_{m,n}/4 - \mathcal{H}(\sigma)/4$ . Thus, indeed, finding the maximum cut partition, configuration  $\sigma$  yielding the maximum of  $\mathcal{C}(\sigma)$ , is equivalent to finding the ground state, configuration  $\sigma$ , at which  $\mathcal{H}(\sigma)$  takes the minimum value.

In dynamical Ising machines [10], the computational properties of classical spin networks are exposed through implementing the networks in various continuous dynamical systems designed or selected with the objective that the system progresses towards a state that is tightly related to the network ground state or, equivalently, to the maximum cut partitioning of the network graph. This is achieved by representing the binary spins by continuous variables,  $\sigma_m \rightarrow \xi_m$ , and associating with the collective state of the dynamical variables a Lyapunov, or more general objective function. The choice of function is constrained by two requirements. First, it should change monotonously on the trajectories of the dynamical system. Second, spin-like states, with  $\xi = \sigma$ , yield the same value of the objective function as its discrete counterpart. For example, if the dynamical system is characterized by a continuous energy function,  $\mathcal{H}_M(\xi)$ , then  $\mathcal{H}_M(\xi = \sigma) = \mathcal{H}(\sigma)$ .

Requiring that the objective function monotonously changes with evolution puts Ising machines into the context of solving optimization problems, which, at present, is a dominating approach to Ising machines. However, the optimization perspective is too broad, and the discrete optimization is famous for ubiquitous hard problems [11, 12]. For example, the general max-cut problem, which is native to Ising machines, besides

being NP-hard is also APX-hard [13], meaning that there is a limit to approximation that can be achieved in polynomial time. Consequently, the Ising machines are commonly regarded as heuristic optimization engines aiming for approximate solutions. This essentially puts Ising machines out of the context of solving “common” information processing tasks that demand exact solutions, even if non-deterministic.

In the present paper, we demonstrate that individual dynamical models driving Ising machines possess a powerful computational resource that allows them to solve certain non-trivial data-processing problems exactly. Specifically, we show that an Ising machine driven by the  $V_2$  dynamical model [14] can solve discrete tomography problem about restoring a binary image from its tomographic data, the collection of pixel sums along a discrete set of rays. Notably, this ability stems from specific dynamical features of the  $V_2$  model, in particular, the ability to traverse spin configurations transcending Hamming-bound constraints.

Our consideration shows that Ising machines can be considered in a much broader context as platforms for realizations of an alternative class of viable algorithms performing “traditional” data-processing tasks.

The rest of the paper is organized as follows. In Section 2, we overview the main properties of the  $V_2$  model. In Section 3, we provide the graph-theoretical formulation of the discrete tomography problem to solve by the  $V_2$  model. In Section 4, we analyze the convergence of the  $V_2$  model to the solutions of the tomography problem.

## 2 Basic properties of the $V_2$ model

The  $V_2$  model is a representative of a broad class of dissipative dynamical systems driving relaxation-based Ising machines.

The  $V_2$  model describes a special class of dynamical systems with dissipative dynamics. The dynamical variables of the system are associated with nodes  $\mathcal{V}$  of undirected finite graph  $\mathcal{G} = \{\mathcal{V}, \mathcal{E}\}$ , whose set of edges  $\mathcal{E}$  with assigned weights (both, positive and negative weights are allowed) represent coupling between the variables. We will denote the distribution of variables associated with the graph nodes by  $\xi = (\xi_1, \dots, \xi_N)$ . The evolution of the system is governed by equations of motion that are convenient to define as  $\dot{\xi} = 2\nabla_\xi \mathcal{C}_{V_2}(\xi)$ , ensuring that  $\mathcal{C}_{V_2}(\xi)$  is a non-decreasing function of time. The  $V_2$  model is defined by

$$\mathcal{C}_{V_2}(\xi) = \frac{1}{4} \sum_{\alpha, \beta \in \mathcal{V}} A_{\alpha, \beta} |\xi_\alpha - \xi_\beta|_{[-2, 2]}, \quad (3)$$

where  $A_{\alpha, \beta}$  is the (weighted) adjacency matrix of graph  $\mathcal{G}$ , and  $|\dots|_{[-2, 2]}$  is a periodic function with period 4 defined for  $-2 \leq \xi \leq 2$  by  $|\xi|_{[-2, 2]} = |\xi|$ .

Taking  $\xi_\alpha = \pm 1$  turns  $\mathcal{C}_{V_2}(\xi)$  into the total weight of edges between the nodes corresponding to  $\xi$ ’s with different signs. In other words,  $\mathcal{C}_{V_2}(\xi)$  is a relaxation of the cut function. In turn, since the system is either at rest, or  $\mathcal{C}_{V_2}(\xi)$  increases with time, the the  $V_2$  model evolution can be related to finding the maximum cut of graph  $\mathcal{G}$ .

The connection with the combinatorial structures emerging on the graph and the  $V_2$  model is made more transparent by employing the periodicity of the kernel

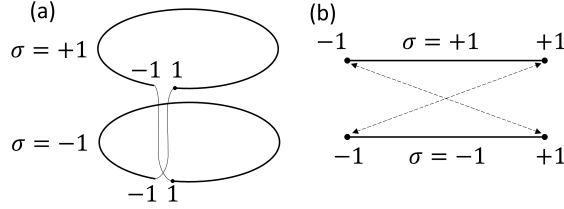


**Fig. 1** The phase space of relaxed spins in the  $V_2$  model as (a) two circles with the transition rule, or, alternatively, as (b) two intervals  $[-1, 1]$  with respectively identified boundary points.

in Eq. (3) and introducing new dynamical variables, relaxed spins, by the relation  $\xi_\alpha = \sigma_\alpha + X_\alpha + 4k_a$ . Here,  $\sigma \in \{-1, 1\}$  and  $X \in (-1, 1]$  are the binary and continuous components of the relaxed spin, respectively. Integer  $k_\alpha$  accounts for the kernel periodicity in  $\mathcal{C}_{V_2}(\xi)$  and plays no role in the following. Rewriting Eq. (3) using the relaxed spin representation, we obtain

$$\mathcal{C}_{V_2}(\sigma, \mathbf{X}) = \mathcal{C}(\sigma) + \tilde{\mathcal{C}}_{V_2}(\sigma, \mathbf{X}), \quad (4)$$

with

$$\tilde{\mathcal{C}}_{V_2}(\sigma, \mathbf{X}) = \frac{1}{4} \sum_{\alpha, \beta} A_{\alpha, \beta} \sigma_\alpha \sigma_\beta |X_\alpha - X_\beta|. \quad (5)$$

Respectively, the dynamics of relaxed spins is governed for  $X_\alpha \in [-1, 1)$  by

$$\dot{X}_\alpha = \sum_{\beta \in \mathcal{V}} A_{\alpha, \beta} \sigma_\alpha \sigma_\beta \operatorname{sgn}(X_\alpha - X_\beta), \quad (6)$$

where  $\operatorname{sgn}(X)$  is the sign function with the adopted convention  $\operatorname{sgn}(0) = 0$ . The evolution described by these equations occurs on the phase space of relaxed spins illustrated by Fig. 1. The topology of the phase space is reflected by supplementing the equations of motion with the rule of negotiating the basepoint in the wedge sum by the phase point: whenever  $X_\alpha$  crosses the  $X = \pm 1$  boundary,  $\sigma_\alpha$  changes sign.

The computational significance of the evolution of dissipative dynamical Ising machines can be established by relating it to the properties of the terminal states of the machine initiated in a generic state. The dynamics governed by Eqs. (6) terminates at critical points of  $\mathcal{C}_{V_2}(\sigma, \mathbf{X})$  that possess several general key features discussed in [14]).

First of all, while the terminal states of the  $V_2$  model are not necessarily binary (the continuous components of the relaxed spins may not vanish in the terminal state), it is trivial to round them optimally because of the vanishing term  $\tilde{\mathcal{C}}_{V_2}(\sigma, \mathbf{X})$  at critical points. The relaxed cut function  $\tilde{\mathcal{C}}_{V_2}(\sigma, \mathbf{X})$  is invariant with respect to global rotations of the phase circles, or, alternatively, global homogeneous translation  $\mathbf{X} \rightarrow \mathbf{X} + r\mathbf{1}$ , with  $\mathbf{1} = (1, 1, \dots, 1)$ , performed on the model phase space with the respective inversions of the binary component of the relaxed spin. Consequently, the binary cut function  $\mathcal{C}(\sigma)$  evaluated in terminal states of  $V_2$  model does not depend on the choice of the (global) origin on the model phase circles. While rotating the phase circles may produce different binary states  $\sigma$ , they all correspond to the same value of

the cut function and, from this perspective, are equivalent. Hence, nonbinary solutions can be mapped to binary states by simply ignoring the continuous component of the relaxed spin. It is worth noting that this is a specific property of the  $V_2$  model. Various relaxations can be productively represented in terms of relaxed spins with the relaxed cut function invariant with respect to global phase rotations. However, the binary states produced by such rotations may yield different cut values raising the special problem of optimal rounding (see, e.g., Section 8.2 in [15]).

The terminal states of the  $V_2$  model have a characteristic structure with relaxed spins grouping into clusters with the same value of the continuous component. This is a consequence of the fact that for states with all continuous component different, the relaxed cut function is a linear function of  $\mathbf{X}$  with the vanishing Hessian. To account for this circumstance, we introduce the notion of *strong clusters*. Critical point  $(\boldsymbol{\sigma}, \mathbf{X})$  partitions the set of graph nodes  $\mathcal{V}$  into a system of  $1 \leq S \leq |\mathcal{V}|$  disjoint subsets (strong clusters)  $\mathcal{V} = \bigcup_{p=1}^S \mathcal{V}^{(p)}(\boldsymbol{\sigma}, \mathbf{X})$  with  $\mathcal{V}^{(p)}(\boldsymbol{\sigma}, \mathbf{X}) = \{\alpha \in \mathcal{V} : X_\alpha = X^{(p)}\}$  and  $X^{(p)} \neq X^{(p')}$  for  $p \neq p'$ . It is convenient to enumerate clusters in such a way that  $X^{(p)} > X^{(p')}$  for  $p > p'$ .

The convergence to a system of strong clusters does not constrain the structure of the terminal states since the definition does not preclude clusters from having only one node. Thus, an arbitrary distribution  $\mathbf{X}$  can be regarded as a system of strong clusters. However, commonly, for instance while solving the discrete tomography problem, in terminal states, all relaxed spins group into a few strong clusters.

Coinciding coordinates in strong clusters require addressing the problems related to discontinuities in the right-hand-side of Eq. (6). We deal with these difficulties using the separability of strong clusters emerging from generic initial conditions and continuity and boundedness of the relaxed cut function. The character of interaction between the relaxed spins in the  $V_2$  model allows one to separate the dynamical contributions stemming from the interactions within the clusters and between the relaxed spins in different clusters, which enables an analysis of the convergence to a system of strong clusters and its stability. To utilize this feature, we introduce *weak clusters*, when groups of relaxed spins can be clearly identified without having all continuous components within a group coinciding. More formally, a system of weak clusters is a partition  $\mathcal{V} = \bigcup_p \mathcal{U}^{(p)}(\boldsymbol{\sigma}, \mathbf{X})$  induced by a system of non-intersecting open intervals  $\mathcal{I}^{(p)} = (X_-^{(p)}, X_+^{(p)}) \subset [-1, 1]$ , such that  $\mathcal{U}^{(p)}(\boldsymbol{\sigma}, \mathbf{X}) = \{\alpha \in \mathcal{V} : X_\alpha \in \mathcal{I}^{(p)}\}$ . We say that a weak cluster is *generic* if all continuous components of the relaxed spins are distinct:  $X_\alpha \neq X_\beta$  for all  $\alpha, \beta \in \mathcal{V}$  such that  $\alpha \neq \beta$ .

The next distinctive property of the relaxed cut function  $\mathcal{C}_{V_2}(\boldsymbol{\sigma}, \mathbf{X})$  is that it has no local maxima: its critical points are either saddle points or max-cut. At the same time, the evolution of the  $V_2$  model can terminate in a saddle point. Identifying such situations is the main problem in investigating the convergence of the  $V_2$  model.

In this regard, another important feature of the  $V_2$  model is worth emphasizing as it greatly enhances the model computational power. While departing from a slight perturbation of a binary state, the system of relaxed spins ends up in a state with the cut not smaller than that of the initial state. More precisely, if the initial state is  $(\boldsymbol{\sigma}(0), \mathbf{X}(0))$ , the  $V_2$  model progresses in such a way that  $\mathcal{C}(\boldsymbol{\sigma}(t)) \geq \mathcal{C}(\boldsymbol{\sigma}(0))$ .

Moreover, if  $\sigma(0)$  does not yield the maximum cut,  $\mathcal{C}(\sigma(0)) < \overline{\mathcal{C}_{\mathcal{G}}}$ , the probability of improving cut by a random perturbation of the continuous component is strictly positive (Theorem 6 in [14]). We will call the randomly agitated  $V_2$ -machine a system, whose dynamics is described by the  $V_2$  model and whose terminal states are randomly agitated.

The beneficial property of random agitations is their ability to break disadvantageous patterns that may emerge due to a peculiar character of the initial condition. For example, the model initialized in state  $(\sigma, \mathbf{0})$  with random  $\sigma$  will stay in this computationally insignificant state. The same trivial result is obtained for an “agitated” initial state of the form  $(\sigma, \kappa \mathbf{1})$ , with  $|\kappa| < 1$ . Random agitations eliminate such pathological effects.

### 3 Graph formulation of discrete tomography

The main distinguishing features of the dynamics of the  $V_2$  model are established in relation to the evolution of a system of relaxed spin on graphs toward their ground state. Therefore, the discussion of how the  $V_2$  model solves the discrete tomography problem significantly benefits from reformulating the latter in graph-theoretical terms.

The discrete tomography envisions a great variety of problems related to reconstructing images from limited information [16, 17]. Here, we focus on the canonical problem of recovering a binary image from its projections along a selected family of rays. Usually, this problem is formulated as follows. The binary image is represented by  $\hat{s}$ , a square  $W \times W$  matrix with elements  $s_{m,n} \in \{0, 1\}$ . The tomographic data is given by two vectors  $\mathbf{P}^{(\text{row})}$  (assigning to each row the sum over columns) and  $\mathbf{P}^{(\text{col})}$  (assigning to each column the sum over rows) with components  $P_m^{(\text{row})} = \sum_n s_{m,n}$  and  $P_n^{(\text{col})} = \sum_m s_{m,n}$ . Solving a tomography problem means reconstructing the binary image from the tomographic data: finding such distribution of set pixels in the  $W \times W$  matrix, whose projections along columns and columns reproduces the tomographic data. It should be noted that, in general, the tomography problem is ill-posed: vectors  $\mathbf{P}^{(\text{row})}$  and  $\mathbf{P}^{(\text{col})}$  do not necessarily define  $\hat{s}$  uniquely [16, 18, 19]. For example, when  $\mathbf{P}^{(\text{row})}$  have coinciding elements, say,  $P_m^{(\text{row})} = P_{m'}^{(\text{row})}$  for some  $m \neq m'$ , then the image obtained by permuting rows  $m$  and  $m'$  also satisfies the same tomographic data but may be different. Since the objective of the present paper is to outline the computational capabilities of the  $V_2$ -machine, we will understand the tomography problem as finding *any* image  $\hat{s}$  that satisfies the tomographic data. From this perspective, it is more important that the tomographic data is *consistent*: there exists at least one image satisfying the data. In what follows, we will assume that this is indeed the case.

Another important condition that we will assume always fulfilled is that the tomographic data is collected along such a system of rays that any two rays may intersect at most at one point. For the example above, this condition is met trivially because each pixel  $s_{m,n}$  contributes only to  $P_m^{(\text{row})}$  and  $P_n^{(\text{col})}$ . Consequently, two distinct pixels  $s_{m,n}$  and  $s_{m',n'}$  contribute to the same tomographic data only if  $m = m'$ ,  $n \neq n'$  or  $m \neq m'$ ,  $n = n'$ .

To reformulate the tomography problem in graph-theoretical terms, we identify the image pixels with with set  $\mathcal{V}$  of nodes and define the binary image

as a function on the nodes:  $\mathbf{s} : \mathcal{V} \rightarrow \{0, 1\}$ . Next, the system of rays,  $\mathcal{R} = \{\mathcal{R}(r) \subset \mathcal{V}, 1 \leq r \leq R : |\mathcal{V}(r) \cap \mathcal{V}(d')| \leq 1, r \neq r'\}$ , is a set of rays  $\mathcal{R}(r)$ , subsets of nodes such that two different subsets have at most one node in common.

The *tomographic data* is a function  $\mathbf{P}_s : \mathcal{R} \rightarrow \mathbb{Z}$  evaluating the pixel-sum along the ray, the total weight of intersection of image  $\mathbf{s}$  with the rays,  $\mathbf{P}_s : \mathcal{R}(r) \mapsto P_s(r) := \sum_{u \in \mathcal{R}(r)} s(u)$ . In other words,  $P_s(r)$  is the number of set pixels in the  $r$ -th ray traversing image  $\mathbf{s}$ . Respectively, the *tomography problem* is posed as finding a binary image  $\mathbf{s}' : \mathcal{V} \rightarrow \{0, 1\}$  with matching tomographic data,  $\mathbf{P}_{s'} = \mathbf{P}_s$ .

In these terms, the canonical formulation corresponds to a set of  $W^2$  nodes arranged as a  $W \times W$  square on a 2D integer lattice, with subsets  $\mathcal{R}(r)$  representing the rows and the columns of the square. At the same time, the generalized formulation covers other classes of besides reconstructing 2D images given the tomographic data collected along the rows and columns of the image. For example, clues specifying pixels that must be set or unset in the reconstructed image can be defined as a tomographic data collected over single-pixel rays. Furthermore, the generalized reformulation naturally extends to problems with a more complex geometry, such as reconstructing 3D images (see Section 5.2 below).

Since the ground state of a spin network is equivalent to a maximum cut partition, we seek for a graph, whose maximum cut corresponds reconstructing the binary image satisfying the tomographic data. To this end, we consider a particular ray  $\mathcal{R}(r) \in \mathcal{R}$  with  $N(r) = |\mathcal{R}(r)|$  nodes and its partitioning given by the spin configuration  $\sigma$ . Associating spins up with set pixels, we find that the reconstructed single-ray image satisfies the tomographic data if  $Q(r; \sigma) := \sum_{\alpha \in \mathcal{R}(r)} \sigma_{\alpha} + \tilde{q}_0(r) \sigma_0 = 0$ , where  $\tilde{q}_0(r) = N(r) - 2P_s(r)$  is the tomographic data written for the spin representation of the binary image and  $\sigma_0 \equiv 1$  is the fixed auxiliary spin. The deviation of the image represented by  $\sigma$  from the tomographic data can be quantified by penalty  $Q^2(r; \sigma)$ , which has a direct combinatorial meaning. With ray  $\mathcal{R}(r)$ , we associate graph  $\tilde{\mathcal{K}}(r)$ , a complete graph  $\mathcal{K}_{\mathcal{R}(r)}$  on  $\mathcal{R}(r)$  with added dominating vertex (auxiliary spin)  $\{0\}$  connected to the rest of the nodes by edges with weight  $\tilde{q}_0(r)$ . We denote by  $\tilde{\mathcal{K}}(r) = \mathcal{R}(r) \cup \{0\}$  the set of nodes in ray  $r$  with added dominating vertex. Configuration  $\sigma$  induces cut of  $\tilde{\mathcal{K}}(r)$  that can be written as  $\mathcal{C}(\sigma)_{\tilde{\mathcal{K}}(r)} = \bar{\mathcal{C}}_{\tilde{\mathcal{K}}(r)} - \frac{1}{4}Q^2(r; \sigma)$ , where  $\bar{\mathcal{C}}_{\tilde{\mathcal{K}}(r)} = (N(r) - P_s(r))^2$  is the maximum cut of  $\tilde{\mathcal{K}}(r)$ .

Extending such consideration to all rays, we find that reconstructing binary image from tomographic data is equivalent to finding the maximum cut partition of graph  $\mathcal{G}_{s, P} = \{\tilde{\mathcal{V}}, \mathcal{E}\}$ , with  $\tilde{\mathcal{V}} = \mathcal{V} \cup \{0\}$ , constructed by the union of cliques  $\tilde{\mathcal{K}}(r)$  with  $r = 1, \dots, R$ . An example of the graph representing a discrete tomography problem on a  $3 \times 3$  grid is shown in Fig. 2.

Depending on the context, it may be convenient either to regard a set of individual auxiliary spins associated with different rays, or to contract all the auxiliary spins to a single dominating vertex. During such a contraction, multiple (or parallel) edges may form because a single node may belong to several rays and hence can be connected to multiple auxiliary nodes corresponding to different cliques. Such multiple edges, in turn, are contracted to a single edge with the accumulated weight. For example, let node  $\alpha$  belong to rays  $\mathcal{R}(r_1)$  and  $\mathcal{R}(r_2)$  with the respective  $\tilde{q}_0(r_1)$  and  $\tilde{q}_0(r_2)$ , then

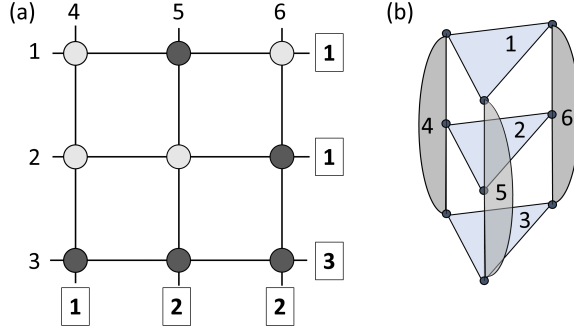


**Fig. 2** An example of a graph representation of a discrete tomography problem. (a) A tomography problem set on  $3 \times 3$  grid. Circles represent pixels, horizontal and vertical lines indicate rays, along which the tomographic data is collected, plain numbers are an enumeration of rays, bold framed numbers are tomographic data for the example image (a glider from Conway's Game of Life [20]) with dark shaded circles representing pixels set ON. (b) A graph corresponding to problem shown in (a). Enumerated shaded regions show cliques representing the corresponding rays and contain auxiliary nodes holding the auxiliary spin.

in  $\mathcal{G}_{s,P}$  with contracted auxiliary spins, node  $\alpha$  is connected to the dominating vertex by the edge with weight  $\tilde{q}_0(r_1) + \tilde{q}_0(r_2)$ .

On the other hand, to find the combinatorial meaning of a solution to the discrete tomography problem, it is convenient to keep the auxiliary spins separated because in this case cliques  $\tilde{\mathcal{K}}(r)$  do not share edges. Consequently, the cut weight produced by partitioning  $\mathcal{G}_{s,P}$  is the sum of cut weights produced by induced partitioning of  $\tilde{\mathcal{K}}_{\mathcal{R}(r)}$ , yielding

$$\mathcal{C}_{\mathcal{G}_{s,P}}(\sigma) = \sum_r \mathcal{C}_{\tilde{\mathcal{K}}(r)}(\sigma) = \bar{\mathcal{C}}_{\mathcal{G}_{s,P}} - \frac{1}{4} \sum_r Q^2(r; \sigma), \quad (7)$$

where  $\bar{\mathcal{C}}_{\mathcal{G}_{s,P}} = \sum_r (N(r) - P_s(r))^2$  is the maximum cut of  $\mathcal{G}_{s,P}$ . Here, we observe that the partitioning yielding the maximum cut of  $\mathcal{G}_{s,P}$  simultaneously delivers the maximum cut of all cliques  $\tilde{\mathcal{K}}_{\mathcal{R}(r)}$ . This is a graph-theoretical formulation of the consistency of the tomographic data, which plays the key role in the following.

Once a problem is formulated as a max-cut problem for a graph with weighted edges, the equations of motion of the  $V_2$  model can be obtained from graph weighted adjacency matrix using Eq. (6). Such an approach may be useful for, say, generating equations of motion for numerical simulations. However, for a productive analysis of the computational capabilities of the  $V_2$  model, it is constructive to reflect the structure of the graph representing the tomography problem directly in the equations of motion. Therefore, we delay writing the explicit form of these equations till the next section [see Eqs. (17) and (18)], where they will be presented in a much more compact form compared to a straightforward explication of Eq. (6).

## 4 Convergence to the solutions

### 4.1 Terminal states for single-ray problems

The computational capabilities of an Ising machine are determined by the properties of terminal states that can be reached with high probability starting from a generic initial state. As discussed above, the only stable critical points of the  $V_2$  model are those yielding the maximum cut of the network, and, strictly speaking, there are no local maxima. However, owing to the structure of the equations of motion, the dynamical system governed by the  $V_2$  model may terminate in a saddle point. The picture significantly simplifies in view of the fact that all critical points of  $\mathcal{C}_{V_2}(\sigma, \mathbf{X})$  belong to critical manifolds enumerable by purely binary states [14]. Therefore, while considering whether a particular terminal state can be reached, the binary component can be considered fixed. States unstable with respect to generic small perturbations can be disregarded. In the worst case, the system can be led away from them by random agitations. As we will see, many saddle critical manifolds can be ruled out based on this simple analysis. However, for some critical manifolds such consideration is not sufficient.

The ground for a more refined analysis is the observation that stability of a critical point is determined by the equations of motion of the same structure as of the equations arising in 1D electrostatics with vector charges. To relate these seemingly different situations, we consider the simplest case when the image is covered by a single ray:  $\mathcal{R} = \{\mathcal{R}(1)\}$  with  $\mathcal{R}(1) = \mathcal{V}$ , or, in other words, graph  $\mathcal{G}_{s, P}$  coincides with clique  $\widetilde{\mathcal{K}}_{\mathcal{R}(1)}$ . In this case, the tomographic data reduces to a single number  $P(1)$ , the number of activated pixels in the image. With each free node  $\alpha \neq 0$ , we associate charge  $q_\alpha = \sigma_\alpha$ , and to the auxiliary node we assign charge  $q_0 = \sigma_0 \tilde{q}(1) = N(1) - 2P(1)$ . Using these notations, equations of motion (6) for free spins can be rewritten in a simple form

$$\dot{X}_\alpha = q_\alpha \epsilon(X_\alpha), \quad (8)$$

where

$$\epsilon(X) = \sum_{\beta: X_\beta < X} q_\beta - \sum_{\beta: X_\beta > X} q_\beta. \quad (9)$$

Here, the summation runs over all spins, including the auxiliary one.

Next, we notice that if we are interested only in establishing the stability of a given spin configuration  $\sigma$ , the system of equations (8) can be regarded as defined on the whole real line. It is straightforward to show that spin distribution  $\sigma(0)$  is stable with respect to perturbation  $\mathbf{X}(0)$ , that is the system initially in state  $(\sigma(0), \mathbf{X}(0))$  terminates in a state with the same discrete component, if and only if the dynamics governed by Eqs. (8) on  $\mathbb{R}$  is bound. Consequently, we can investigate the stability of relaxed-spin distributions characterized by the fixed distribution of the discrete component  $\sigma$  by using the framework of stability in the Lyapunov sense.

Finally, we observe that the stability of solutions of Eqs. (8) on  $\mathbb{R}$  is equivalent to stability of a system of charged particles on 1D (or a system of parallel charged planes) with the same charges,  $q_i$ , as defined above for the relaxed spins, and the particle corresponding to the auxiliary spin fixed at the origin. The equivalence follows from the observation that, up to the choice of time scale, the right-hand-side of the

equations of motion governing the charged particles has the same form,  $q_\alpha \epsilon(X_\alpha)$ , as in Eqs. (8) and (9). The distinguishing feature of the equations of motion for charged particles is that they are a system of the *second* order differential equations. However, from the stability perspective, this distinction is only technical and plays a minor role.

From this perspective, the penalty associated with missing the tomographic constraint can be written as  $Q(\sigma) = \sum_{\alpha \in \tilde{\mathcal{K}}(r)} q_\alpha$  and interpreted as the total ray charge. Respectively, it is constructive to define charges of other collections of relaxed spins, such as strong and weak clusters. For instance, we obviously have that if a weak cluster converges to a strong cluster, then they have the same charge.

When the tomographic constraint is met, the ray charge is zero,  $Q(\sigma) = 0$ . Since the tomography problem has a solution, the zero value is feasible. Then, it is not difficult to see that  $Q(\sigma)$  may take only even values. This, simple but important, observation together with the analogy with stability of a system of electric charges immediately yield a key property.

**Theorem 1** *For a single ray tomography problem, states with  $Q(\sigma) = 0$  (the solutions of the problem) are the only stable states of the  $V_2$  model. Moreover, starting from a generic initial state,  $V_2$  model terminates in a  $Q(\sigma) = 0$  state.*

The first part of the theorem is a simple consequence of the fact that at equilibria of the  $V_2$  model, the relaxed and discrete cut function coincide, and equilibria are either max-cut states or are saddle points. If a terminal state is a max-cut state, then  $Q\sigma = 0$ , and  $\sigma$  delivers a solution to the single-ray tomography problem. If the system terminates in a saddle point, then, due to continuity of  $\mathcal{C}_{V_2}(\sigma, \mathbf{X})$ , there exist variations of the continuous component of the relaxed spin increasing  $\mathcal{C}_{V_2}(\sigma, \mathbf{X})$ . After such displacements, the motion is unbounded because it must lead to a variation of the discrete component of the relaxed spin [14].

The second part of the theorem can be regarded as following from Earnshaw's theorem about stability of a system of charges from electrostatics [21] or can be proven directly by respectively adapting the usual argument used to prove Earnshaw's theorem. We start from a useful technical statement

**Lemma 1** *Let a weak generic cluster  $\mathcal{V}^{(p)}$  occupying interval  $(X_-^{(p)}, X_+^{(p)})$ , such that either  $X_-^{(p)} > 0$  or  $X_+^{(p)} < 0$  (so that  $\mathcal{V}^{(p)}$  does not contain the auxiliary spin) have sufficiently high charge,  $|Q^{(p)}(\sigma)| > 1$ , where  $Q^{(p)}(\sigma) = \sum_{\alpha \in \mathcal{V}^{(p)}} q_\alpha$ . Then  $\mathcal{V}^{(p)}$  is unstable.*

*Proof* According to Eq. (9), the equations of motion governing the relaxed spins inside  $\mathcal{V}^{(p)}$  are determined by the field  $\epsilon(X_\alpha)$  that can be written as

$$\epsilon(X_\alpha) = \epsilon^{(\bar{p})} + \epsilon^{(p)}(X_\alpha), \quad (10)$$

where  $\epsilon^{(\bar{p})}$  and  $\epsilon^{(p)}(X_\alpha)$  are the contributions due to the relaxed spins inside and outside of  $\mathcal{V}^{(p)}$ , respectively. Since  $|Q^{(p)}| \geq 2$ , there are two distinct relaxed spins in  $\mathcal{V}^{(p)}$  with the

charge  $q^{(p)}$  of the same sign as  $Q^{(p)}$  and extremal values of their  $X$ -coordinates among the relaxed spins in  $\mathcal{V}^{(p)}$  with the same charge. Let these marginal relaxed spins be  $\beta$  and  $\gamma$ , and  $X_- < X_\beta < X_\gamma < X_+$ . Then, we have

$$\frac{d}{dt} (X_\gamma - X_\beta) = q^{(p)} \left[ \epsilon^{(p)}(X_\gamma) - \epsilon^{(p)}(X_\beta) \right] = 2q^{(p)} \left[ q^{(p)} + \sum_{\alpha: X_\beta < X < X_\gamma} q_\alpha \right] > 0. \quad (11)$$

The inequality follows from comparing the expression in the square brackets with the total charge of  $\mathcal{V}^{(p)}$ .

Thus, the separation between  $\beta$  and  $\gamma$  increases leading to either unbound evolution or collision with other clusters.  $\square$

*Proof of Theorem 1* The whole set of relaxed spins can be regarded as a weak cluster with a charge of even (including zero) magnitude. To apply Lemma 1, we need to incorporate the auxiliary spin with its fixed continuous component.

The argument used for proving Lemma 1 would be invalidated if the auxiliary spin is the only carrier of the excess charge. It is easy to show, however, that this is impossible. Without loss of generality, we can assume that the excess charge is positive,  $Q(\sigma) > 0$ . Now, suppose the auxiliary spin with  $q_0 > 0$  is the only positively charged particle, so that all free relaxed spins have  $q_\alpha = -1$ . However, in this case, the total charge is  $q_0 + \sum_{\alpha \neq 0} q_\alpha = N - 2P - N = -2P \leq 0$ , which contradicts the assumption that  $Q(\sigma) > 0$ .

What remains to be checked is how Eq. (11) changes when one of the marginal relaxed spins is the auxiliary spin. Let  $Q(\sigma) > 0$ , and the auxiliary spin with  $q_0 > 0$  and relaxed spin  $\beta$  with  $X_\beta > 0$ , are positively charged relaxed spins with the smallest and the largest continuous component, respectively. Then, we have

$$\frac{dX_\beta}{dt} = q_\beta \left[ \sum_{\alpha: X < X_\beta} q_\alpha - \sum_{\alpha: X > X_\beta} q_\alpha \right] \geq q_\beta [Q(\sigma) - q_\beta] > 0, \quad (12)$$

where we have taken into account that  $|Q(\sigma)|$  is even. Equation (12) is intentionally written in the form valid for both  $Q(\sigma) > 0$  and  $Q(\sigma) < 0$  cases. It is elementary to adopt the argument to the case when  $X_\beta < 0$  and to show that in this case  $dX_\beta/dt < 0$ .

Thus, generic weak clusters can only converge to a strong cluster if they represent a solution of the tomography problem.  $\square$

We conclude the analysis of the single-ray case by noting that except for the cases with all pixels set or unset, single-ray tomography problems have multiple solutions [14]. In this case, the terminal state can be expected to consist of multiple strong clusters. Since Lemma 1 is applicable to each cluster independently, we obtain that the resultant strong clusters must have zero charge. In particular, this implies that if a strong cluster does not contain the auxiliary spin, then, generically, it should comprise only two relaxed spins.

## 4.2 Terminal states for multiple rays

A generalization of the approach in the previous section to tomography problems with  $R > 1$  rays requires accounting for the fact that the relaxed spins belonging to different rays do not interact with each other. This is achieved by associating with the relaxed spins vector charges defined in the  $R$ -dimensional Euclidean space. To this

end, in  $\mathbb{R}^R$ , we introduce basis vectors  $\vec{e}(r)$  with coordinates  $\vec{e}(r)_j = \delta_{r,j}$ . Next, for each relaxed spin  $\alpha$  we introduce  $\mathcal{D}(\alpha) = \{r : \alpha \in \mathcal{R}(r)\}$ , the set of rays containing  $\alpha$ . Finally, we define the vector charge for a free relaxed spin  $\alpha \neq 0$

$$\vec{q}_\alpha = \sigma_\alpha \sum_{r \in \mathcal{D}(\alpha)} \vec{e}(r). \quad (13)$$

Respectively, for the auxiliary spin, we define

$$\vec{q}_0 = \sum_{r \in \mathcal{D}(\alpha)} \tilde{q}_0(r) \vec{e}(r). \quad (14)$$

Using these definitions, one can define vector charges of collections of relaxed spins as a sum of vector charges. For example, the total vector charge carried by state  $(\sigma, \mathbf{X})$  is  $\vec{Q}(\sigma) = \sum_{\alpha \in \mathcal{V}} \vec{q}_\alpha$ , while the total charge of relaxed spins in ray  $r$  is natural to define as  $\vec{Q}(r; \sigma) = \sum_{\alpha \in \mathcal{R}(r)} \vec{q}_\alpha$ . In terms of vector charges, the cut weight of graph  $\mathcal{G}_{s,p}$  [Eq. (7)] takes a simple form

$$\mathcal{C}_{\mathcal{G}_{s,p}}(\sigma) = \bar{\mathcal{C}}_{\mathcal{G}_{s,p}} - \frac{1}{4} \vec{Q}(\sigma) \cdot \vec{Q}(\sigma), \quad (15)$$

where  $\vec{a} \cdot \vec{b}$  denotes the inner product in Euclidean space. Equation (15) is obtained directly from Eq. (7) by noticing that  $Q(r; \sigma) = \vec{e}(r) \cdot \vec{Q}(\sigma) = \vec{e}(r) \cdot \vec{Q}(r; \sigma)$ .

Respectively, the relaxed cut function [Eq. (4) written for the discrete tomography problem] is written as

$$\mathcal{C}_{V_2}(\sigma, \mathbf{X}) = \mathcal{C}_{\mathcal{G}_{s,p}}(\sigma) + \frac{1}{4} \sum_{\alpha, \beta} \vec{q}_\alpha \cdot \vec{q}_\beta |X_\alpha - X_\beta|. \quad (16)$$

Finally, the equations of motion governing the  $V_2$  model are a straightforward generalization of Eqs. (8) and (9):

$$\dot{X}_\alpha = \vec{q}_\alpha \cdot \vec{\epsilon}(X_\alpha), \quad (17)$$

where

$$\vec{\epsilon}(X) = \sum_{\beta: X_\beta < X} \vec{q}_\beta - \sum_{\beta: X_\beta > X} \vec{q}_\beta. \quad (18)$$

A substantial technical deviation from the single-ray case is expressed by the fact that in the vector case, the formal equilibrium corresponds not only to the case of vanishing vector field but also to the case of orthogonal  $\vec{q}_\alpha$  and  $\vec{\epsilon}(X_\alpha)$ . Dynamically, the orthogonality expresses the exact cancellation of the contributions originating from different rays containing the relaxed spin. Such cancellation invalidates an important property self-evident in the single-ray case that in equilibrium there are no isolated relaxed spins.

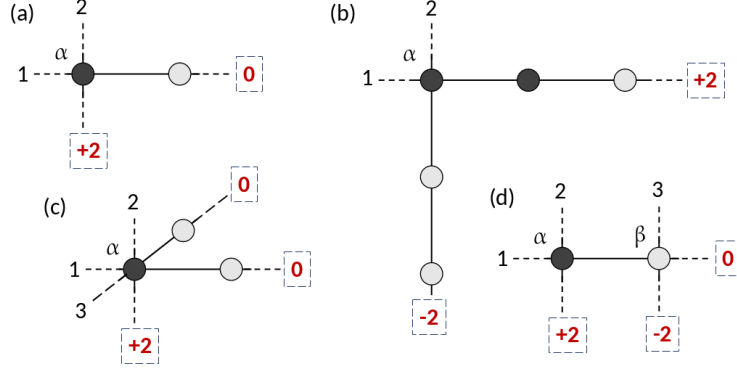


**Fig. 3** Examples of configurations violating the tomographic data that are stable equilibria for the relaxed spin  $\alpha$ . Dashed-framed numbers show deviations of the respective components of the vector charge from zero due to mismatched tomographic data. Circles depict states of the discrete components that need to be corrected. (a) Spin  $\alpha$  is in neutral equilibrium. (b) Spin  $\alpha$  is asymptotically stable (there is a returning field acting on  $\alpha$ ). Five spins need to be corrected to match the tomographic data. (c) A configuration similar to (a) but at the intersection of three rays. Spin  $\alpha$  is asymptotically stable state, while only three spins need to be corrected. (d) A realization of the configuration from (a) for a tomography problem on a 2D grid leads to violating the tomographic data in two rays. Both  $\alpha$  and  $\beta$  are in neutral equilibrium.

The accidental orthogonality can be eliminated by ensuring that projections  $\vec{e}(r) \cdot \vec{Q}(r)$  for different  $r$  are linearly independent over  $\{-1, 1\}$ . In our simulations, such linear independence was forced by redefining the last term in Eq. (16) as  $\frac{1}{4}\vec{Q}(\sigma) \cdot \Lambda \cdot \vec{Q}(\sigma)$ , where  $\Lambda = \text{diag}(\lambda(1), \dots, \lambda(R))$  is a diagonal matrix with positive linearly independent  $\lambda(r) > 0$ . Alternatively, this procedure can be understood as redefining  $\vec{e}(r) \rightarrow \sqrt{\lambda(r)}\vec{e}(r)$ . In computations, it was sufficient to generate the diagonal elements as  $\lambda_r = \sqrt{p(r)}/[\sqrt{p(r)}]$ , where  $\{p(r)\}$  is a set of random distinct prime numbers.

Satisfying the tomographic data for the  $r$ -th ray results in  $\vec{e}(r) \cdot \vec{Q}(r) = 0$ . This provides a way for translating the results obtained in the previous section to the multi-ray case and identifying the main barriers for converging to a reconstructed image starting from generic initial conditions and the dynamical features of the  $V_2$  model that allow overcoming these barriers.

The conclusion that the  $V_2$  states  $(\sigma, \mathbf{X})$  with  $\sigma$  satisfying the tomographic data are the only stable terminal states remains valid for the problems with multiple rays as well. As discussed above, this follows from the fact that the relevant critical points of  $\mathcal{C}_{V_2}(\sigma, \mathbf{X})$  besides max-cut are saddle points.

On the other hand, the argument used for proving the second part of Theorem 1 is invalid. This reflects the fact that for multiple-ray tomography problems, Earnshaw's-like statements about instability of *individual* charges are no longer true for vector charges. As demonstrated by Fig. 3, there do exist arrangements of vector charges stable with respect to any single-particle disturbances. Respectively, to match the tomographic data in the presence of these patterns requires inversion of *multiple* spins.

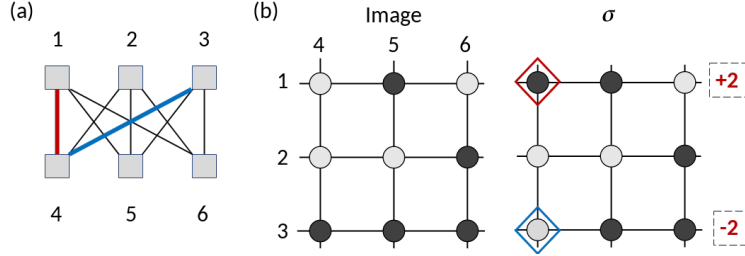


**Fig. 4** (a) An example of the ray graph  $\mathcal{G}_R$  for the discrete tomography problem on the  $3 \times 3$  grid. The highlighted edges show edge-induced subgraph  $\mathcal{I}_R(\sigma'|\sigma) \subseteq \mathcal{G}_R$ . (b) An example of a  $3 \times 3$  image and an incorrect spin configuration stable with respect to single-spin perturbations. Correction of the selected spins is represented by  $\mathcal{I}_R(\sigma|\sigma)$  shown in (a).

Consequently, local search-based approaches to solve the spin formulation of the discrete tomography problem are prone to terminate in states with such defects as manifested in numerical simulations shown in Section 5.1.

In turn, inherently, the  $V_2$  model's trajectories are not constrained to Hamming-limited variations of the discrete component of the relaxed spin [14]. As a result, the  $V_2$ -machine can either avoid defects or escape them after the random agitation of a terminal state breaking the tomographic data.

To discuss this property of the  $V_2$  model, we limit ourselves to the tomography problem on a 2D rectangular grid, where the typical defects in terminal states stable with respect to single-particle perturbations have the form shown in Fig. 3. It is not difficult to see that such patterns lead to mismatching the tomographic data in, at least, two rays.

**Lemma 2** *For a tomographic problem on a rectangular grid, if the spin configuration  $\sigma$  does not match the tomographic data,  $\vec{Q}(\sigma) \cdot \vec{Q}(\sigma) > 0$ , then there are at least two rays with unsatisfied tomographic data.*

*Proof* We represent the system of rays by graph  $\mathcal{G}_R$ , whose nodes correspond to rays, and two nodes are connected if the respective rays intersect. For example, the graph representing the tomography problem for a  $W \times W'$  image is a complete bipartite graph  $\mathcal{K}_{W,W'}$  with partitions,  $\mathcal{A}$  and  $\mathcal{B}$ , corresponding to rows and columns, respectively (see Fig. 4). We notice that the edges in this graph correspond to the image pixels. Indeed, two rays intersect only at a single pixel, and each pixel lies at the intersection of at most two rays, thus there is a bijection between pixels and the edge set of  $\mathcal{G}_R$ . Having such correspondence established, we assign to the edges weights  $\pm 1$  according to the value of the respective spins. In other words, we regard the spin configuration  $\sigma$  as defining a function  $\sigma : \mathcal{E}(\mathcal{G}_R) \rightarrow \{-1, 1\}$ .

Let the tomographic constraint be broken in ray  $r_1$  by having one too many set pixels, so that  $Q(r_1; \sigma) = \vec{e}(r_1) \cdot \vec{Q}(r_1; \sigma) = 2$ . Let the error be correctable by inverting relaxed spin  $\alpha \in \mathcal{R}(r_1)$  with  $\sigma_\alpha = 1$ . This relaxed spin lies at the intersection of rays  $\mathcal{R}(r_1)$  and  $\mathcal{R}(r_2)$  and, by assumption,  $Q(r_2; \sigma) = 0$ . Thus, there another relaxed spin  $\beta \in \mathcal{R}(r_2) \cap \mathcal{R}(r_3)$  with  $\sigma_\beta = -1$  must be inverted together with  $\sigma_\alpha$  to maintain zero error in  $\mathcal{R}(r_2)$ . Consequently, there exists relaxed spin  $\gamma \in \mathcal{R}(r_3) \cap \mathcal{R}(r_4)$  with  $\sigma_\gamma = 1$  that must be inverted to maintain zero error in  $\mathcal{R}(r_3)$ , and so on.

This observation shows that a transformation from the configuration  $\sigma$  to a correct configurations  $\sigma'$  selects a subset of edges in  $\mathcal{G}_{\mathcal{R}}$  corresponding to the set of spins that need to be inverted. This subset defines an edge-induced subgraph  $\mathcal{T}_{\mathcal{R}}(\sigma) \subseteq \mathcal{G}_{\mathcal{R}}$ . For each node  $\mathcal{R}(r) \in \mathcal{T}_{\mathcal{R}}(\sigma'|\sigma)$ , the total variation of  $Q(r; \sigma)$  is equal to the doubled total weight of the edges incident to  $\mathcal{R}(r)$ . Since, as was discussed above, the tomographic data may not uniquely define the image, there may be multiple graphs  $\mathcal{T}_{\mathcal{R}}(\sigma)$  describing the respective correcting transformations. Since, by the main assumption, the tomography problem has a solution, there exists at least one such graph, which is sufficient for our purposes.

First, we notice that if the degree of  $\mathcal{R}(r)$  for some  $r$  is odd, then  $|Q(r; s)| > 0$ . But there must be an even number of nodes with odd degree in a graph, implying the lemma.

It remains to consider the case when  $\mathcal{T}_{\mathcal{R}}(\sigma)$  is Eulerian. It is worth noticing that due to the even degrees, they correspond to correcting configurations  $\sigma$  with strong violations of the tomographic constraint,  $|Q(r; \sigma)| \geq 4$ , which, as follows from the proof of Lemma 1, cannot emerge from weak clusters.

For Eulerian  $\mathcal{T}_{\mathcal{R}}(\sigma)$  the multiplicity of rays mismatching the tomographic data follows from the fact that there are no odd cycles in  $\mathcal{T}_{\mathcal{R}}(\sigma)$ . To employ this property, we introduce an orientation of edges in  $\mathcal{T}_{\mathcal{R}}(\sigma)$ . Without loss of generality, we assume that the tomographic constraint is broken in ray  $\mathcal{R}(r_1) \in \mathcal{A}$  and  $Q(r_1; \sigma) > 0$ . Then, we define edges with positive and negative weights as oriented from  $\mathcal{A}$  to  $\mathcal{B}$  and from  $\mathcal{B}$  to  $\mathcal{A}$ , respectively. Then, due to the absence of odd cycles, any directed cycle defines such a set of relaxed spins whose inversion does not change the ray charges and, therefore, cannot correct the mismatched tomographic data. Such directed cycles can be removed without loosing the property of  $\mathcal{T}_{\mathcal{R}}(\sigma)$  to describe a correcting transformation.

Next, we construct a directed trail starting from  $\mathcal{R}(r)$  following the orientation of the incident edges. Any return to  $\mathcal{R}(r)$  defines a directed cycle, which can be removed from  $\mathcal{T}_{\mathcal{R}}(\sigma)$  without exhausting the edges outgoing from  $\mathcal{R}(r)$ . Without directed cycles, a directed trail starting from  $\mathcal{R}(r)$  must terminate at another ray  $\mathcal{R}(r')$  with an imbalance between incoming and outgoing edges and, hence,  $|Q(r'|\sigma)| > 0$ .

It is worth noticing that the case of Eulerian  $\mathcal{T}_{\mathcal{R}}(\sigma)$  corresponds to strong violations of the tomographic constraint,  $|Q(r|\sigma)| \geq 4$  and  $|Q(r'|\sigma)| \geq 0$ . Adapting the argument used in the proof of Lemma 1, it can be shown that the respective configurations  $\sigma$  cannot emerge from a weak cluster.  $\square$

In view of Lemma 2, we limit ourselves to considering the simplest case of a defect shown in Fig. 3(d) and showing that random agitations can lead to rearranging of both spins  $\alpha$  and  $\beta$  eliminating errors in both rays. It is not difficult to see that it is sufficient that after the random agitation, relaxed spins  $\alpha$  and  $\beta$  both have, say, positive continuous components maximal compared to other relaxed spins in rays containing  $\alpha$  and  $\beta$ . Indeed, in this case, the equations of motion of these relaxed spins take the form

$$\begin{aligned} \frac{dX_\alpha}{dt} &= \vec{q}_\alpha \cdot \left( \vec{Q}(\sigma) - \vec{q}_\alpha - \vec{q}_\beta \right) + \vec{q}_\alpha \cdot \vec{q}_\beta \operatorname{sgn}(X_\alpha - X_\beta), \\ \frac{dX_\beta}{dt} &= \vec{q}_\beta \cdot \left( \vec{Q}(\sigma) - \vec{q}_\alpha - \vec{q}_\beta \right) + \vec{q}_\alpha \cdot \vec{q}_\beta \operatorname{sgn}(X_\beta - X_\alpha). \end{aligned} \quad (19)$$

Taking into account that  $\vec{Q}(\sigma) = 2(\vec{q}_\alpha + \vec{q}_\beta)$ , we find

$$\frac{d}{dt} (X_\alpha + X_\beta) = (\vec{q}_\alpha + \vec{q}_\beta)^2 > 0. \quad (20)$$

Considering other particles in the rays containing  $\alpha$  and  $\beta$  with the  $X$ -coordinates taking the maximal (after excluding  $\alpha$  and  $\beta$ ) value, one can easily check that they are non-increasing. Thus,  $\alpha$  and  $\beta$  remain outsiders with increasing  $X$ -coordinates, hence their motion is unbound. For the  $V_2$  model evolution, this implies that both spins  $\alpha$  and  $\beta$  will invert, which eliminates the error in recovering the image.

## 5 Numerical demonstrations

The theoretical framework developed above shows the origin of the the  $V_2$  model capability to solve discrete tomography problem. At the same time, solving practical tomography problems requires much more than recovering *an* image from tomographic data. For example, one may impose additional constraints on the recovered image (see, e.g. [22]) or accounting for possible errors in the tomographic data itself [23], and so forth. In the present paper, we limit ourselves to demonstrations of the basic capabilities of the  $V_2$  model on two simplified examples: reconstructing 2D and 3D images. The evolution of the  $V_2$  model was simulated using the Euler approximation supplied with the rule of updating the binary component of the relaxed spin as illustrated in Fig. 1. While the Euler approximation is not trouble-free and may lead to emergence of various artifacts [24], it is sufficient for our purposes in the present paper. In all the examples, the  $V_2$ -machine ran unsupervised without any additional processing and only random agitations were applied.

### 5.1 Tomography of 2D binary images

As the first demonstration, we studied the probability  $P_{\text{succ}}$  of successful reconstruction of an image from its tomographic data on a set of random square binary images with the sides varying from 4 to 30. For each size, five images were generated with the probability  $p = 0.5$  of a pixel to be activated. For both approaches,  $P_{\text{succ}}$  was obtained by averaging over the set of five images.

In results shown in Fig. 5, the  $V_2$ -machine time measured in the inverse units used in the equations of motion (17) and was limited to  $T = 5.0$  between agitations for the results shown in Fig. 5(a) (the number of agitations was limited to 10) and changed in the interval [2.0, 5.3] for Fig. 5(b) (the number of agitations was fixed to 5). The wall-time required by a hardware of a software implementation to process one agitation depends on such details as the duration of the time steps in the Euler approximation and organization of computation. The simulations used a fixed number,  $M = 600$ , of time steps with the duration of  $\Delta t = \frac{T}{M}$ . For each time-step, the computations used the sparsity of the graph  $\mathcal{G}_{s,P}$ . Thus, the time complexity of the  $V_2$  simulations shown in Fig. 5 can be estimated as  $\mathcal{O}(MW^3)$ , where  $W$  is the width of the field, per one agitation stage. An efficient parallelization of computations can be expected to reduce the wall-time scaling to  $\mathcal{O}(MW)$  per agitation stage.

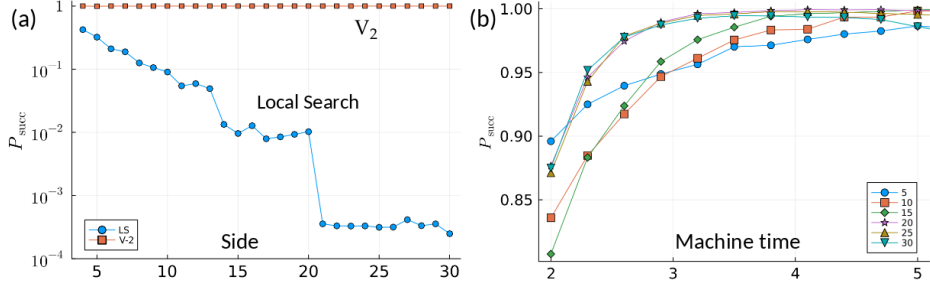


**Fig. 5** Probability of successful reconstruction of images  $P_{\text{succ}}$  from the tomographic data for square random binary images. (a) Comparison of  $P_{\text{succ}}(W)$  as a function of the image side length,  $W$ , for two approaches: using the  $V_2$  model and 1-opt local search. (b) The variation of  $P_{\text{succ}}$  with the duration of the free evolution stage between random agitations for random images of selected sizes: 5, 10, 15, 20, 25, 30.

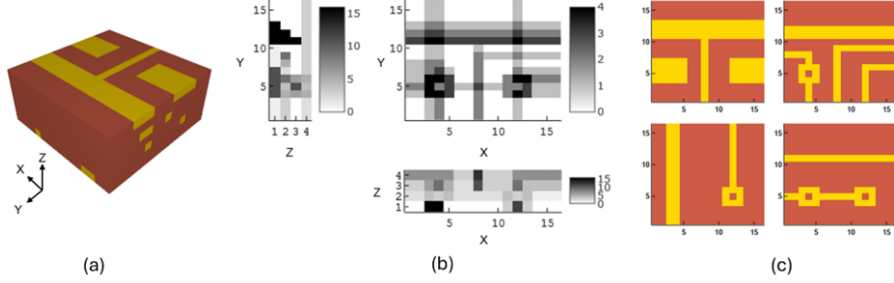
Figure 5(a) compares two approaches to recovering an image from its tomographic data using the spin-based formulation of the tomography problem: using the  $V_2$  model and 1-opt local search (greedy search) that ensures that in the terminal state the cut weight cannot be improved by inverting any single spin. The success probability was sampled for the  $V_2$  model by restarting it from 100 random initial conditions. Since the successful recovery by the local search turns with increasing the image size into a rare event, for the local search,  $P_{\text{succ}}$  was sampled by restarting it from  $10^6$  random initial states. While studying the performance of local search on a spin representation of the discrete tomography problem is not our objective, we would like to notice a curious behavior of  $P_{\text{succ}}(W)$ : it drops significantly when the most probable total mismatch with the tomographic data increases by two, or the number of defects like shown in Fig. 3(d) increases by one, but changes only moderately between these transitions.

Figure 5(a) demonstrates the inherent complexity of the discrete tomography problem. Its spin representation does not determine whether an image can be successfully recovered from its tomographic data by a particular implementation of the Ising machine. The ability of the  $V_2$  model to solve the tomography problem is a result of its specific dynamical properties, as discussed in the previous sections.

To provide a better illustration of how the dynamics of the  $V_2$  model affects the solution of the tomography problem, Fig. 5(b) shows the dependence of  $P_{\text{succ}}$ , obtained from sampling terminal states obtained from  $10^3$  random initial conditions, on duration of the evolution between random agitations. This dependence demonstrates the emergence of several universal dynamical features, such as the universal convergence of  $P_{\text{succ}}$  to 1 at  $T \approx 3.5$ , whose investigation is a subject of ongoing research. It should be noted that as the number of time steps covering the whole interval between the random agitations was kept constant,  $M = 600$ , for all situations, the errors related to the duration the size of the time step become apparent for larger images at  $T \gtrsim 5.0$ .

## 5.2 Tomography of 3D binary images

As a demonstration of advanced capabilities of the  $V_2$  dynamics, we consider reconstruction of a multi-layered printed circuit board. This problem has a straightforward



**Fig. 6** (a) External view of a 4-layered PCB; (b) model tomographic data collected along  $X$ ,  $Y$  and  $Z$  dimensions; (c) reconstructed PCB layers

connection with the general discrete tomography problem, as any PCB (printed circuit board) without integrated circuit chips and other discrete elements can be modelled a three-dimensional binary matrix composed of elements  $\{0, 1\}$ , where ‘1’ represents the presence of conducting material. We restrict the scale of this demonstration so that the number of required spins is in the order of  $10^3$  and hence, consider the reconstruction of small enough 4-layered PCB, such that the maximum size of the projection image is  $16 \times 16$  pixels. Moreover, we assume that the ray projection data is available along only three dimensions of the object.

Figure 6a shows the section of an artificial 4-layered PCB we consider for reverse engineering with the conducting tracks depicted in yellow and the non-conducting base in brown. Figure 6b shows the mock tomographic data of the PCB along in the  $XY$ ,  $YZ$ , and  $ZX$  planes. We obtain this by summing up the discrete binary matrix modelling the PCB in Fig. 6a along three dimensions. Figure 6c shows reconstructed PCB layers.

## 6 Conclusion

We investigated the capability of a relaxation-based dynamical Ising machine driven by the  $V_2$  dynamical model to solve the discrete tomography problem about recovering a binary image from its tomographic data, the pixel sum along a discrete set of rays.

We show that in the simplest single-ray case, the convergence of the  $V_2$  model is governed by the same principles as stability of a system of electrostatically interacting charged particles in 1D. Based on this observation, we show that the  $V_2$  model terminates in a solution to the tomography problem starting from generic initial conditions.

We generalized this approach to the multiple-ray case by identifying a vector charge with the relaxed spins. We identified the main bottleneck terminal states that do not solve the tomography problem, but the  $V_2$  may converge to. We show that random agitations can move the system away from these states, and, as the numerical simulations show, only a few such agitations are needed to ensure the convergence with a high probability ( $P_{\text{succ}} \approx 1$ ). Two key properties of the  $V_2$  model are responsible for this. First, random agitations do not worsen the spin configuration in the terminal state of the system of the relaxed spins. Second, spin transitions occurring during the

evolution of the  $V_2$  model are not Hoffman-limited. This should be contrasted to local search-based treatments of the spin reformulation of the discrete tomography problem, for which such transitions present a strong barrier and lead to the quick deterioration of performance with the problem size manifested in numerical simulations.

Our consideration demonstrates that specific dynamical models can be approached as unconventional algorithms producing exact solutions to highly nontrivial data processing tasks. This advances the conventional approach to dynamical Ising machines, regarding them as heuristic devices targeting approximate solutions to optimization problems.

## Acknowledgements

The work was partially supported by the US National Science Foundation (NSF) under Grant No. 2531175 and partially No. 1909937.

## References

- [1] Kirkpatrick, S., Gelatt, C. D. & Vecchi, M. P. Optimization by Simulated Annealing. *Science* **220**, 671–680 (1983).
- [2] Hopfield, J. J. Neurons with graded response have collective computational properties like those of two-state neurons. *Proceedings of the National Academy of Sciences* **81**, 3088–3092 (1984).
- [3] Černý, V. Thermodynamical approach to the traveling salesman problem: An efficient simulation algorithm. *Journal of Optimization Theory and Applications* **45**, 41–51 (1985).
- [4] Fu, Y. & Anderson, P. W. Application of statistical mechanics to NP-complete problems in combinatorial optimisation. *Journal of Physics A: Mathematical and General* **19**, 1605–1620 (1986).
- [5] Kochenberger, G. A., Glover, F. & Wang, H. in *Binary Unconstrained Quadratic Optimization Problem* (eds Pardalos, P. M., Du, D.-Z. & Graham, R. L.) *Handbook of Combinatorial Optimization* 533–557 (Springer, New York, NY, 2013).
- [6] Barahona, F. On the computational complexity of Ising spin glass models. *Journal of Physics A: Mathematical and General* **15**, 3241–3253 (1982).
- [7] Karp, R. M. in *Reducibility among Combinatorial Problems* (eds Miller, R. E., Thatcher, J. W. & Bohlinger, J. D.) *Complexity of Computer Computations* 85–103 (Springer US, Boston, MA, 1972).
- [8] Garey, M., Johnson, D. & Stockmeyer, L. Some simplified NP-complete graph problems. *Theoretical Computer Science* **1**, 237–267 (1976).

- [9] Lucas, A. Ising formulations of many NP problems. *Frontiers in Physics* **2**, 5 (2014).
- [10] Mohseni, N., McMahon, P. L. & Byrnes, T. Ising machines as hardware solvers of combinatorial optimization problems. *Nature Reviews Physics* **4**, 363–379 (2022).
- [11] Papadimitriou, C. H. & Steiglitz, K. *Combinatorial Optimization: Algorithms and Complexity* Corr. unabridged republication edn (Dover publ, Mineola (N.Y.), 1998).
- [12] Arora, S. & Barak, B. *Computational Complexity: A Modern Approach* (Cambridge University Press, Cambridge, 2009).
- [13] Garey, M. & Johnson, D. *Computers and Intractability. A Guide to the Theory of NP-completeness* (W. H. Freeman and Company, New York, NY, 1990).
- [14] Erementchouk, M., Shukla, A. & Mazumder, P. Self-contained relaxation-based dynamical Ising machines (2023). [arXiv:2305.06414](https://arxiv.org/abs/2305.06414).
- [15] Punnen, A. P. (ed.) *The Quadratic Unconstrained Binary Optimization Problem. Theory, Algorithms, and Applications* (Springer Nature Switzerland AG, Gwerbestrasse, Switzerland, 2022).
- [16] Herman, G. T. & Kuba, A. (eds) *Discrete Tomography: Foundations, Algorithms, and Applications* Applied and Numerical Harmonic Analysis (Birkhäuser Boston, Boston, MA, 1999).
- [17] Herman, G. T. & Kuba, A. (eds) *Advances in Discrete Tomography and Its Applications* Applied and Numerical Harmonic Analysis (Birkhäuser, Boston, 2007).
- [18] Ryser, H. J. in *Combinatorial Properties of Matrices of Zeros and Ones* (eds Gessel, I. & Rota, G.-C.) *Classic Papers in Combinatorics* 269–275 (Birkhäuser, Boston, MA, 1987).
- [19] Gale, D. in *A Theorem on Flows in Networks* (eds Gessel, I. & Rota, G.-C.) *Classic Papers in Combinatorics* 259–268 (Birkhäuser, Boston, MA, 1987).
- [20] Gardner, M. *Wheels, Life and Other Mathematical Amusements* (W. H. Freeman, New York, 1983).
- [21] Griffiths, D. J. *Introduction to Electrodynamics* 4 ed edn (Cambridge university press, Cambridge, 2017).
- [22] Gardner, R. & Gritzmann, P. Discrete tomography: Determination of finite sets by X-rays. *Transactions of the American Mathematical Society* **349**, 2271–2295 (1997).

- [23] Ceko, M. *et al.* Error Correction for Discrete Tomography. *Fundam. Inf.* **189**, 91–112 (2022).
- [24] Shukla, A., Erementchouk, M. & Mazumder, P. Non-binary dynamical Ising machines for combinatorial optimization (2024). [arXiv:2412.08481](https://arxiv.org/abs/2412.08481).